



Analysis of clear-sky Antarctic snow albedo using observations and radiative transfer modeling

Peter Kuipers Munneke,¹ Carleen H. Reijmer,¹ Michiel R. van den Broeke,¹
Gert König-Langlo,² Piet Stammes,³ and Wouter H. Knap³

Received 29 November 2007; revised 3 March 2008; accepted 21 May 2008; published 10 September 2008.

[1] A radiative transfer model for studying spectral and broadband snow surface albedo has been applied to radiation data (1998–2001) from different climate regimes in Antarctica. The model makes use of the doubling-adding method for radiative transfer, combined with the correlated k -distribution technique to account for atmospheric gas absorption. Snow layers are described by scattering phase functions for irregular hexagonal plate-shaped ice crystals. Multiple scattering is included, as well as the option to include soot in the snowpack, as well as clouds. Sensitivity experiments show that the model is capable of calculating spectral and broadband albedos as a function of solar zenith angle and effective snow grain radius r_e . The novel approach of applying the model to multiple-year field data of clear-sky albedo from five locations in Dronning Maud Land, Antarctica, reveals that seasonal clear-sky albedo variations (0.77–0.88) are dominantly caused by strong spatial and temporal variations in r_e . Summer season averages of r_e range from 22 μm on the Antarctic plateau to 64 μm on the ice shelf. Maximum monthly values of r_e are 40–150% higher. Other factors influencing clear-sky broadband albedo are the seasonal cycle in solar zenith angle (at most 0.02 difference in summer and spring/autumn albedo) and the spatial variation in optical thickness of the cloudless atmosphere (0.01 difference between ice shelves and plateau). The seasonal cycle in optical thickness of the atmosphere was found to be of minor importance (<0.005 between summer and spring/autumn).

Citation: Kuipers Munneke, P., C. H. Reijmer, M. R. van den Broeke, G. König-Langlo, P. Stammes, and W. H. Knap (2008), Analysis of clear-sky Antarctic snow albedo using observations and radiative transfer modeling, *J. Geophys. Res.*, 113, D17118, doi:10.1029/2007JD009653.

1. Introduction

[2] Snow-covered ice sheets and glaciers reflect most of the incoming solar radiation, resulting in a high albedo (α) of the snow surface (typically 70–85%). Yet the shortwave radiation balance plays a dominant role in the summer energy balance of the polar snow surface [e.g., Van As *et al.*, 2005]. The amount of absorbed shortwave radiation, being proportional to $1 - \alpha$, is very sensitive to small changes in the snow albedo. It is therefore vital to understand what factors have a strong influence on snow albedo and which have not. The central goal of this paper is to identify and quantify these factors. For this purpose, we will present a detailed radiative transfer model, in which the sensitivity of snow surface albedo to various physical processes can be studied both spectrally and integrated over the shortwave spectrum

(broadband). Once the most important physical processes underlying albedo variations are identified, parameterizations can be made for use in, e.g., mass balance or general circulation models.

[3] Snow surface albedo has been a widely studied subject for decades. A systematic account of a radiation and polar meteorology experiment is documented by Liljequist [1956], in which dependence of broadband snow albedo on snow grain size (r_e), solar zenith angle (θ_0), and cloud cover was already noted. An early integrated field study of snow albedo, θ_0 and cloud cover was carried out by Rusin [1961]. The first comprehensive, analytical model for spectral snow albedo was put forward by Wiscombe and Warren [1980], starting with the single-scattering properties of snow grains. A multiple scattering model for the calculation of radiative transfer in the complete atmosphere–snow system was put forward by Aoki *et al.* [1999]. Their model is very similar in setup to the model we apply here. Both models make it possible to calculate not only spectral, but also broadband albedos. We pursue here the application of the model to four years of continuous field measurements (1998–2001). This provides a deeper understanding of the most relevant causes of variations in albedo in the field.

¹Institute for Marine and Atmospheric Research, Utrecht University, Utrecht, Netherlands.

²Alfred Wegener Institute for Polar and Marine Research, Bremerhaven, Germany.

³Royal Netherlands Meteorological Institute, De Bilt, Netherlands.

[4] The aim of this paper is threefold: (1) to describe briefly the design of the radiative transfer model (section 2), (2) to show the validity of the model doing modeling experiments (section 3), and (3) to show that the model can be applied to field data in order to reveal contributions of different processes to surface albedo changes (section 4). For this model application, we used radiation data gathered at Neumayer station, and by four automatic weather stations (AWSs) situated in various climatic regimes in Dronning Maud Land, Antarctica (see map in Figure 5).

2. Model Description

2.1. Definitions

[5] The radiation field (described by the intensity vector \mathbf{I}_λ) in a medium is a function of zenith angle θ , azimuth angle ϕ , and wavelength λ . The amount of radiation of wavelength λ arriving at the snow surface E_\downarrow (monochromatic irradiance) can be expressed in terms of the radiation field at the surface:

$$E_\downarrow(\lambda) = \int_0^{\frac{\pi}{2}} d\theta \int_0^{2\pi} d\phi \mathbf{I}_\lambda(\theta, \phi) \sin \theta \cos \theta \quad (1)$$

Similarly, the reflected radiation $E_\uparrow(\lambda)$ can be defined. The spectral surface albedo $\alpha(\lambda)$ is then defined as the ratio of reflected and incoming radiation at a wavelength λ :

$$\alpha(\lambda) = \frac{E_\uparrow(\lambda)}{E_\downarrow(\lambda)} \quad (2)$$

Incoming broadband shortwave radiation SW_\downarrow is defined here as the radiation between $\lambda_1 = 250$ and $\lambda_2 = 4,000$ nm:

$$SW_\downarrow = \int_{\lambda_1}^{\lambda_2} d\lambda E_\downarrow(\lambda) \quad (3)$$

Analogously, the reflected broadband shortwave radiation SW_\uparrow is defined using $E_\uparrow(\lambda)$. The albedo for broadband shortwave radiation α (hereafter referred to as broadband albedo) is then given by

$$\alpha = \frac{SW_\uparrow}{SW_\downarrow} = \frac{\int_{\lambda_1}^{\lambda_2} d\lambda E_\uparrow(\lambda) \alpha(\lambda)}{\int_{\lambda_1}^{\lambda_2} d\lambda E_\downarrow(\lambda)} \quad (4)$$

The broadband albedo of the snow surface is *not* an inherent property of the snow. It depends on the radiation field arriving at the surface, which may in turn depend on the zenith angle of the sun, the absorption and scattering by atmospheric gases, aerosols and clouds. The calculation of spectral and broadband albedo therefore requires a radiative transfer model that includes the atmosphere. The numerical model we will use for that purpose is described in the next sections.

2.2. The Radiative Transfer Model DAK

[6] For calculations of the scattering and absorption of light in an atmosphere containing gases, water droplets or ice crystals, and aerosols, we make use of the radiative transfer model DAK (Doubling-Adding KNMI (Royal Netherlands Meteorological Institute)) [De Haan *et al.*, 1987; Stammes *et al.*, 1989; Stammes, 2001]. The model is a numerical imple-

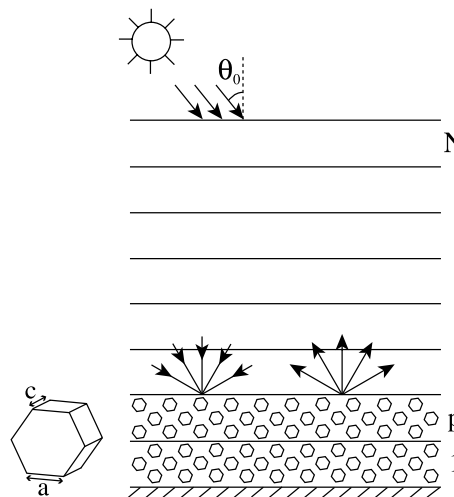


Figure 1. Schematic setup of the DAK model for studying spectral and broadband snow surface albedo. Solar radiation incident at the top of atmosphere has a solar zenith angle θ_0 . The lowermost p layers are filled with snow, consisting of hexagonal ice crystals with dimensions c and a . The snow surface albedo is calculated from the radiation field at the upper boundary of the p th layer. The total number of layers for the atmosphere including snow layers is N .

mentation of the doubling-adding method, the principles of which have been introduced by Van de Hulst [1963]. It calculates the polarized radiation field in a 1-D plane-parallel atmosphere consisting of N homogeneous layers, including multiple scattering of light within and between model layers (see Figure 1).

[7] The model is 1-D in the sense that the spatial coordinate in the vertical direction is the only one considered: it describes a plane-parallel atmosphere, in which all properties of the layers are assumed to be homogeneous in the horizontal directions. At each model layer boundary however, the radiation field is calculated three-dimensionally: as a function of the zenithal and azimuthal directions.

[8] The assumption that the model layers are flat potentially leads to serious inaccuracies at low solar elevations. Therefore we applied an Earth curvature correction, which effectively places the sun a bit higher (up to 2° for $\theta_0 > 80^\circ$), thus reducing the air mass along the path of the direct solar radiation [Kasten and Young, 1989]. Refraction effects in a curved atmosphere are still not accounted for, however.

[9] Absorption by gas molecules, and scattering and absorption by atmospheric aerosols, dependent on wavelength λ , is taken care of by DAK. Rayleigh scattering by atmospheric gases is incorporated using the formula given by Stam *et al.* [2000]. Vertical profiles of gas concentrations, temperature and pressure are prescribed.

2.3. Correlated k -Distribution Method

[10] DAK originally is a monochromatic model: it calculates the absorption and scattering by particulate media at a single wavelength only. The amount of absorption by atmospheric gases varies strongly with wavelength, however. Furthermore, it depends on the temperature and pressure of the gases constituting the atmosphere. If the entire

shortwave spectrum (250–4,000 nm) is to be analyzed at a resolution sufficient to capture the irregular patterns of gas absorption bands, it would require several thousands of monochromatic line-by-line calculations. To avoid this computationally costly approach, we have implemented the correlated k -distribution method for gaseous absorption in DAK.

[11] The correlated k -distribution method [e.g., *Lacis and Oinas, 1991*] allows for the computation of gas absorption of an entire wavelength interval using only a few radiative transfer calculations. The key aspect of the k -distribution method is to reorder the absorption coefficients in a wavelength interval in order of increasing magnitude, instead of by wavelength. The resulting smooth functions, called cumulative probability functions, can be adequately approximated by a numerical Gaussian quadrature method involving only a few (typically 5–16) spectral quadrature points (i.e., radiative transfer calculations). By using the same Gaussian spectral quadrature for every atmospheric layer, the k -distribution method is said to be ‘correlated.’ A thorough mathematical treatment is provided by *Thomas and Stamnes* [1999, Ch. 10].

[12] The construction of the cumulative probability functions does initially require line-by-line calculations for each wavelength interval. This has been done by *Kato et al.* [1999], who made them available through the libRadtran software package (<http://www.libradtran.org>). They subdivided the shortwave spectrum into 32 wavelength intervals that closely follow absorption bands of the gases CO₂, O₂, O₃, and H₂O. For each gas in each wavelength interval, they generated lookup tables of absorption coefficients k as a function of temperature and pressure, for each Gaussian quadrature point. The absorption coefficients of water vapor are also dependent on the water vapor concentration itself.

[13] In this study, DAK has been extended with numerical procedures that (1) retrieve the absorption coefficients from the lookup tables by *Kato et al.* [1999] using pressure, temperature, and water vapor concentration, and (2) calculate and store the radiation field for all spectral quadrature points, ultimately adding these to get the final radiation fluxes for the wavelength interval.

[14] All other calculations in a wavelength interval, e.g., for molecular scattering, are performed at the central wavelength of that wavelength interval. In this work, we use the first 29 of the 32 wavelength intervals (240–3,001 nm) as the solar radiation intensity above 3,000 nm is very small. It also allows us to compare model calculations to observations from pyranometers, which have a spectral range of 300–3,000 nm. The UV range from 240 to 300 nm, by which model and observations differ, is characterized by strong Rayleigh scattering and ozone absorption, practically eliminating its contribution to irradiance calculations at the surface.

[15] Figure 2 illustrates how the combination of DAK and the correlated- k method can simulate gaseous absorption bands in the atmosphere. Transmission is higher when θ_0 is small due to the reduced path through the atmosphere.

[16] Spectral surface albedo is returned by DAK as the surface albedo in each of the 29 wavelength bands (equation (2)). The broadband albedo is calculated using

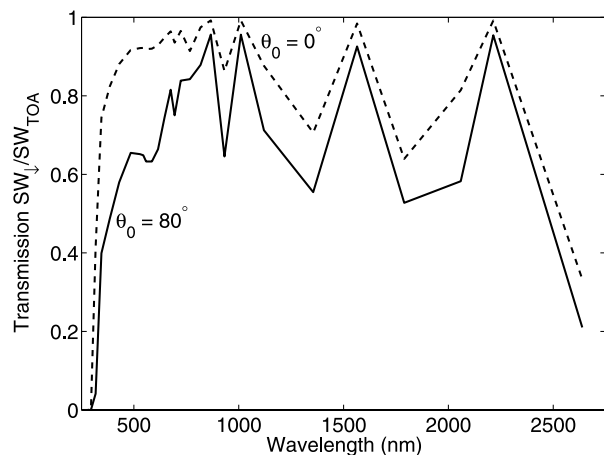


Figure 2. Spectral transmission of the atmosphere with a surface albedo of zero for all wavelengths, plotted for solar zenith angles $\theta_0 = 0^\circ$ and $\theta_0 = 80^\circ$.

equation (4), where the integral is replaced by a summation over the 29 wavelength bands.

2.4. The Model Snowpack

[17] In this study, snow is treated as a particulate medium consisting of mutually independent ice crystals. The ice crystals can be either of spherical or (imperfect) hexagonal shape. The optical properties of a snow layer are captured with a volume absorption coefficient, a single scattering albedo, and a scattering phase function (SPF). The absorption coefficient is derived using the imaginary part of the refractive index of ice [*Wiscombe and Warren, 1980*], updated with data from *Warren et al.* [2006] for the UV/visible range. The SPFs of hexagonal ice crystals are calculated using the ray-tracing program SPEX written by *Hess et al.* [1998], as opposed to *Aoki et al.* [1999] who used traditional Mie scattering calculations. The SPFs are consequently expanded in generalized spherical harmonics following the method by *De Rooij and van der Stap* [1984]. These expansion coefficients are used in DAK. Since the scattering of solar radiation by snowflake-sized ice crystals is dominantly in the forward direction, the SPF is calculated using the delta approximation [*Potter, 1970*] with a cutoff angle of 1° . We found that our results of radiative transfer calculations through a snowpack do not change significantly when we increase the cutoff angle to more than 1° (unpublished). Optionally, soot can be prescribed to the snowpack, but we will not use that option in this study (see section 5.1).

[18] The lowermost p layers of DAK are given optical properties of a snow layer by assigning the SPF, single scattering albedo, and optical thickness. The p snow layers together are chosen to be so opaque that virtually no radiation arrives at the lower model boundary (for a 10 m snow layer, the optical thickness is $>2 \times 10^6$). The requirement to prescribe a surface albedo to this lower model boundary has become irrelevant in this way: the surface albedo of the snowpack can now be studied independently by looking at the up- and downward radiation fluxes at the uppermost boundary of the p th layer. This approach has been taken as well by, e.g., *Aoki et al.* [1999].

Table 1. List of Model Parameters for All Runs in This Study (Default Values) Unless Specified Otherwise

Parameter	Symbol	Value
No. of radiation bands		29
Wavelength range	λ_1	240 nm
	λ_2	3001 nm
Absorptive gases		H ₂ O, CO ₂ , O ₂ , O ₃
No. of Gauss points		5–16
No. of zenith angles		72 (144 streams)
No. of azimuth angles		30
SPF cutoff angle		1°
Ice crystal aspect ratio	Γ	0.2
No. of model layers	N	33
No. of snow layers	p	1 (10 m)
Snow density	ρ	350 kg m ⁻³

[19] Throughout this work, we assume the snowpack to consist of ice crystals shaped like irregular hexagonal plates. Although we are unaware of publications on the typical aspect ratio $\Gamma (=c/2a)$ of Antarctic snow crystals, we take it to be 0.2, where c is the central axis of the plate (its “thickness”), and a the length of each of the sides of the hexagon (Figure 1). Irregularity refers to some distortion of the crystal faces. It is obtained by, within limits, changing the surface normal randomly while performing the ray-tracing calculations [see Macke *et al.*, 1996; Hess *et al.*, 1998; Knap *et al.*, 2005].

[20] To facilitate comparison with other literature, snow grain size will be expressed by the quantity r_e , best described as the optically equivalent snow grain size [e.g., Nolin and Dozier, 2000; Legagneux *et al.*, 2006; Matzl and Schneebeli, 2006]. It refers to the radius of a spherical particle that has the same volume to surface ratio as the hexagonal ice plate.

[21] The settings of the model as used in this study are summarized in Table 1.

3. Model Sensitivity Study

[22] In this section, we present results of various numerical experiments in which the snow grain size r_e , and the solar

zenith angle θ_0 are varied, and the effect on the snow surface albedo is calculated.

[23] All experiments in this section were carried out using a standard subarctic summer atmosphere [Anderson *et al.*, 1986]. Other settings are summarized in Table 1. Similar results, using spherical ice particles only, have been presented by Aoki *et al.* [1999] and Wiscombe and Warren [1980]. The difference between the latter and our study is the atmospheric part determining the irradiances arriving at the snow surface.

3.1. Snow Grain Size and Solar Zenith Angle

[24] In Figure 3, we show the spectral and broadband albedos of snow for different r_e and θ_0 , as calculated by DAK. An examination of various sources done by Wiscombe and Warren [1980] suggests that fine, new snow has a radius of 20–100 μm . Older, fine-grained snow has a radius of 100–300 μm . For the application to Antarctic data, we present results for $r_e = 50, 100$ and 200 μm .

[25] Mie scattering theory predicts that the larger a particle, the more of the scattered light is directed in the forward direction. Snow consisting of large grains will scatter the incoming solar radiation further into the snowpack than snow consisting of small grains. Effectively, the path length of the radiation through the snowpack increases for larger grains. As the radiation passes through more ice when the path length is increased, the albedo will drop, both spectral and broadband. This behavior is reproduced by our ray-tracing snowpack, both for spectral (Figure 3a) and broadband (Figure 3b) albedo. The decrease of the spectral albedo as a function of r_e is most noticeable in the near-IR above 800 nm. The broadband albedo for a given θ_0 is about 0.06 higher for $r_e = 50 \mu\text{m}$ than for $r_e = 200 \mu\text{m}$.

[26] We compare our spectral albedo curves with measurements at Antarctic snow done by Grenfell *et al.* [1994] in Figure 3a. For a grain size of 100 μm , the visible part of the model albedo agrees well with their measurement data. The near-IR albedos are somewhat underestimated however. Grenfell *et al.* [1994] and Flanner *et al.* [2007] noted exactly the same discrepancy and found that the inclusion of a

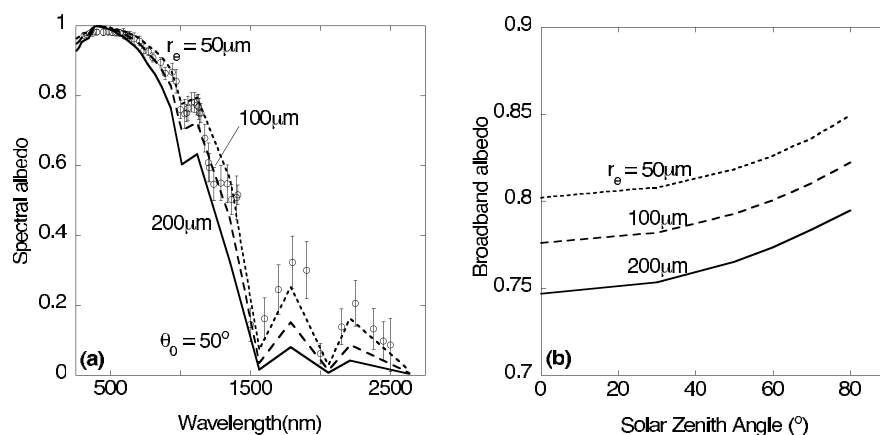


Figure 3. (a) Spectral albedo as a function of wavelength, for snow particles with different effective radii r_e . Circles and corresponding error bars are measurements of spectral albedo reported by Grenfell *et al.* [1994] for Antarctic snow. (b) Broadband albedo as a function of solar zenith angle for the same snow particles as in Figure 3a.

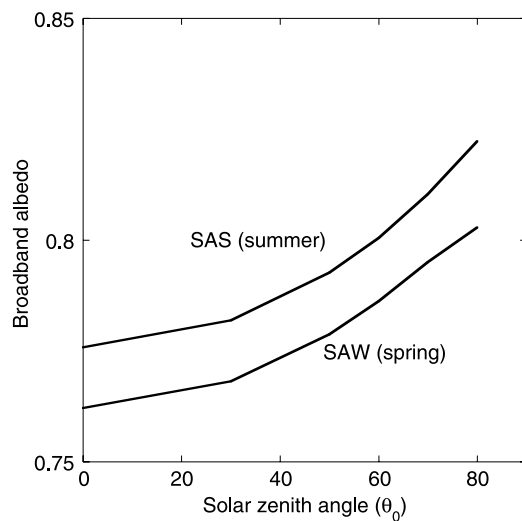


Figure 4. Broadband albedo as a function of solar zenith angle. SAS, AFGL subarctic summer atmosphere; SAW, AFGL subarctic winter atmosphere. The SAW atmosphere may be assumed to represent Antarctic spring conditions.

submillimeter layer of very small snow grains ($30 \mu\text{m}$) can resolve the difference. They argue that vertical heterogeneity in snow grain size can have strong influence on different spectral regions of albedo. We will not use this submillimeter layer in our study. As a result, a vertically constant r_e can match a measured broadband albedo, but it will likely underestimate visible albedo and overestimate near-IR albedos somewhat.

[27] The solar zenith angle θ_0 has two effects on both the spectral and broadband albedo. First, for large θ_0 , the incoming solar radiation is less likely to penetrate deep into the snow, so the path length through the snow is shortened, increasing the albedo. Second, at very large θ_0 , the radiation becomes almost exclusively diffuse. Diffuse radiation has an effective θ_0 of about 50° [Wiscombe and Warren, 1980]. This second effect counteracts the first one, but only at $\theta_0 > 80^\circ$ [Wiscombe and Warren, 1980]; it is not visible in Figure 3b.

3.2. Optical Thickness and Water Vapor Column

[28] Throughout the year, water vapor is the most strongly varying absorbing gas in the (polar) atmosphere. Measurements on Antarctica [e.g., Van den Broeke et al., 2004a] reveal a factor 5 to 10 difference between summer and winter surface specific humidity. This is primarily due to the strong dependence of water vapor concentration on temperature through the Clausius–Clapeyron relation. As water vapor absorption bands are concentrated in the near-IR, the broadband (spectrally integrated) albedo at the ground may increase when the water vapor column is thicker. The magnitude of this effect is demonstrated in Figure 4 as the two solid lines, showing two model runs with a standard subarctic summer and subarctic winter atmosphere [Anderson et al., 1986]. For all θ_0 , the difference in broadband albedo is about 0.013.

[29] This effect can also be caused by differences in surface elevation. High on an ice sheet plateau, the atmosphere

contains far less water vapor than in coastal regions or on ice shelves.

4. Analysis of Clear-Sky Surface Albedo in Antarctica

[30] The model for the atmosphere and snow surface enables us to identify and quantify the physical processes responsible for variation in the albedo measurements in the field. We intend to give a physical explanation for the large-scale, seasonal variations in observed snow surface albedo. For this reason, we have collected field and model data as described below, and compiled these to monthly averages.

[31] We selected the radiation data available from five different locations in Dronning Maud Land, Antarctica. One of these locations is Station Neumayer, which has been delivering high-quality, year-round measurements to the Baseline Surface Radiation Network (BSRN) [Ohmura et al., 1998] since 1994. The other four locations are automatic weather stations (AWSs) that have been collecting both radiation and meteorological data autonomously since 1998 [Van den Broeke et al., 2004a].

[32] After a description of the five locations and their data sets, we will present a data analysis of the observed snow surface albedo, and quantify processes that may lay behind its variability on seasonal time scales using DAK.

4.1. Locations

[33] Station Neumayer, an Antarctic base operated by Germany since 1981, is situated in Dronning Maud Land ($70^\circ37'S$, $8^\circ22'W$), on the Ekström Ice Shelf at 42 m above sea level (Figure 5). The Ekström Ice Shelf has a homogeneous and flat surface with a very small slope upward to the south. A thorough description of the climatology of Neumayer is available in König-Langlo et al. [1998].

[34] IMAU has been employing more than 10 AWSs (numbered AWS 1, 2, etc.) in Antarctica over the past decade. We chose a set of four of these that cover distinct climatic regions in Dronning Maud Land, and that have a data record of appreciable length:

[35] 1. AWS 4 ($72^\circ45.2'S$, $15^\circ29.9'W$, 34 m a.s.l.) on the Riiser-Larsen Ice Shelf, about 80 km from the ice shelf front,

[36] 2. AWS 5 ($73^\circ06.3'S$, $13^\circ09.9'W$, 363 m a.s.l.) just inland of the Riiser-Larsen Ice Shelf grounding line on the coastal slope of the East Antarctica Ice Sheet,

[37] 3. AWS 6 ($74^\circ28.9'S$, $11^\circ31.0'W$, 1160 m a.s.l.) in the escarpment region near Heimefrontfjella, characterized by persistent katabatic winds,

[38] 4. AWS 9 ($75^\circ00.2'S$, $0^\circ00.4'E$, 2892 m a.s.l.) on the East Antarctic Plateau (Amundsenisen).

[39] Surface melt only occurs at Station Neumayer and AWSs 4 and 5, very infrequently between November and February, usually for only one day or a few days at a time. Surface melt at AWS 4 and 5 amounts to $19 \text{ mm w.e. a}^{-1}$ for the period 1998–2001 [Van den Broeke et al., 2004b]. One short event was observed at AWS 6 in the four years considered here, in mid-January 1999.

4.2. Data Description and Treatment

[40] For this study, data from 1 January 1998 to 31 December 2001 (4 years) were selected. Post-2001 data from the AWSs used in this study have not yet been

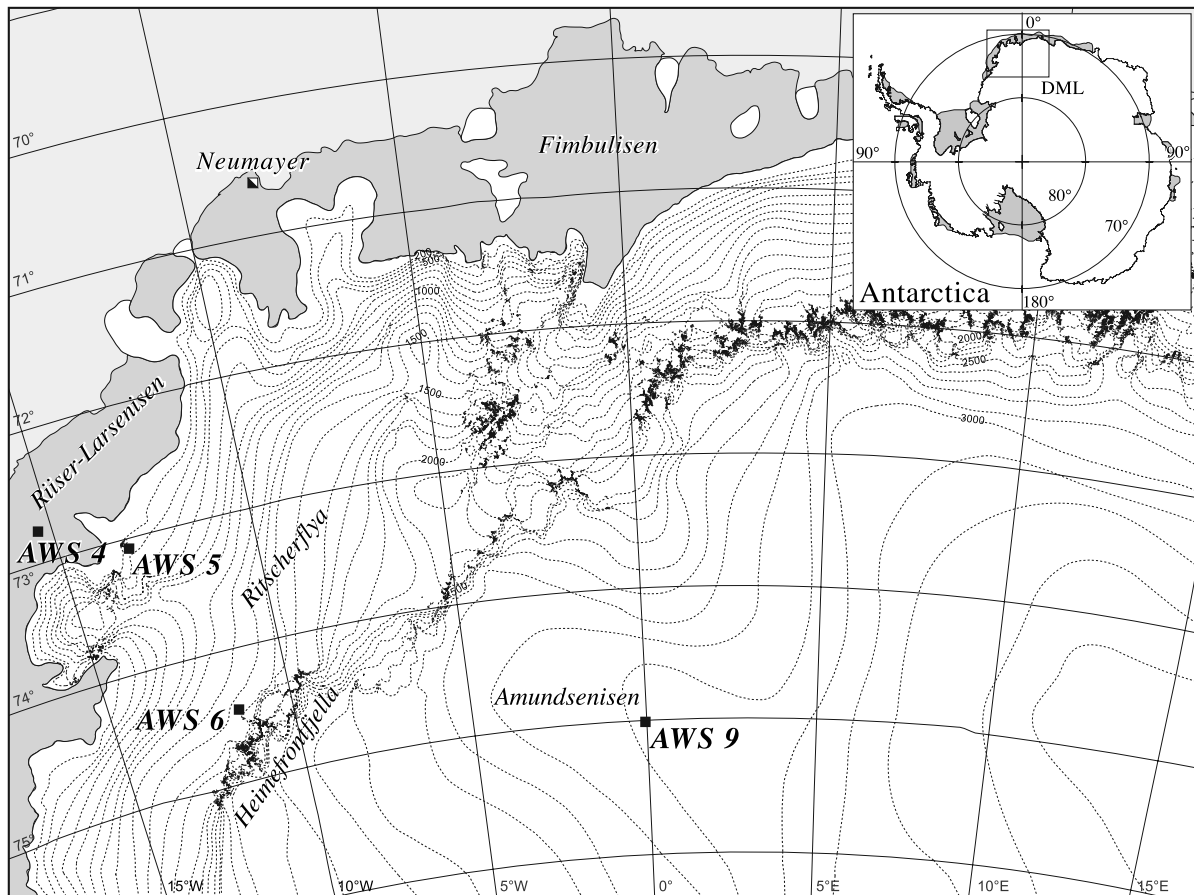


Figure 5. Location of Station Neumayer and the four AWSs, Dronning Maud Land, East Antarctica. Elevation contours are plotted at 100-m intervals.

analyzed thoroughly enough for inclusion in this study. Hourly values of meteorological observations and radiation measurements are available for all measurement locations [e.g., König-Langlo and Herber, 1996; Van den Broeke *et al.*, 2004a]. From Neumayer, year-round, three-hourly synoptic observations of the meteorological conditions according to WMO standards are available, including a description of snow drift. We exclude data between April and September, when the solar elevation is so low that the quality of the data and model performance are challenged.

[41] It should be noted that the data from Neumayer, being a year-round manned research station, is considered superior to the data from the AWSs, which collect data autonomously and get serviced only once a year. Various data processing techniques have been applied to improve the AWS data sets [Van den Broeke *et al.*, 2004c], and especially daily and monthly averages of data are considered to be of good quality.

4.2.1. Radiation Data and Selection of Clear Days

[42] The observed incoming and outgoing shortwave radiation at the surface have a considerable variability at hourly resolution. This is mainly due to rapid changes in cloud cover, wind speed and associated snow drift. Moreover, the pyranometers have a poor cosine response at very large θ_0 , reducing their reliability above $\theta_0 = 80^\circ$. Especially when calculating the surface albedo using individual pairs of

hourly SW_{\uparrow} (reflected shortwave radiation) and SW_{\downarrow} (global shortwave radiation), the errors in the albedo values become rather large at higher θ_0 . We therefore resorted to daily averages, whereby the albedo averaged over 24 h is calculated using the daily accumulated SW -fluxes.

[43] Daily averages of cloud cover n are estimated using the longwave (LW) fluxes, for consistency also at Neumayer where synoptic observations are being carried out. Despite extreme care, synoptic observations do suffer from some subjectiveness. Moreover, synoptically obtained cloud cover may not always reflect the governing radiation balance, e.g., when the sky is fully covered with very thin clouds through which the sun disk is still visible, or when a thin layer of fog is present close to the surface.

[44] We calculated 24-h-averaged cloud cover by plotting LW_{net} ($= LW_{\uparrow} + LW_{\downarrow}$) against LW_{\uparrow} (see Figure 6). Positive fluxes are defined toward the surface. We fit a parabola and a straight line to the 5th and 95th percentile of daily averaged LW_{\uparrow} [see also Van den Broeke *et al.*, 2004c, 2006]. The highest percentile corresponds to the most cloudy days ($n = 1$), as the snow surface is in thermal equilibrium with the warm cloud base under cloudy conditions: then LW_{net} is approximately zero. The lowest percentile of the data points correspond to the days with clearest sky ($n = 0$). A linear interpolation between the two fitted lines gives an estimate of the fractional cloud cover for

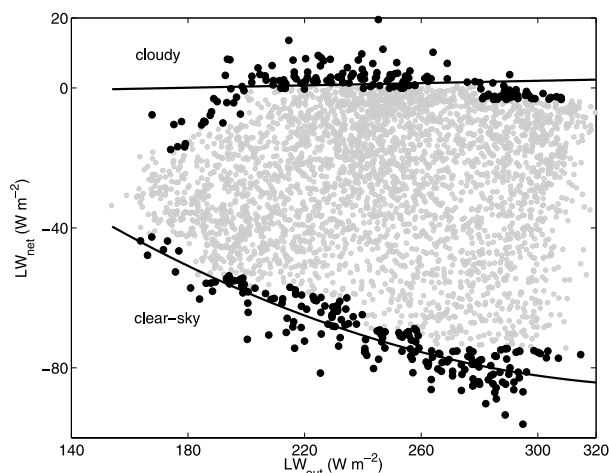


Figure 6. Diurnal averages of net longwave radiation LW_{net} at the surface versus upwelling longwave radiation LW_{\uparrow} for the data set of Station Neumayer. A straight line and a parabola were fitted to the 95th and 5th percentiles, respectively, binned in 20 W m^{-2} intervals of LW_{\uparrow} .

all data points. From the total data set, a clear-sky ($n < 0.2$) subset is distilled, which are from now on referred to as clear days, or as clear-sky conditions. The choice for $n = 0.2$ is arbitrary from a physical point of view, but necessary for a data set of sufficient size.

4.2.2. Vertical Atmospheric Profiles

[45] The vertically integrated water vapor content in the atmosphere varies strongly from month to month, due to its strong dependence on air temperature. In order to take into account the resulting seasonally varying optical thickness of the atmosphere, a vertical profile of temperature, pressure, and specific humidity is prescribed for each month for each location. These vertical profiles are extracted from the 25-year model run with RACMO2/ANT, a regional atmospheric climate model at $\sim 55 \text{ km}$ horizontal resolution, adapted to Antarctic conditions [Van den Berg et al., 2006]. To select only clear-sky profiles, vertically integrated cloud content from the RACMO2/ANT model was used as a criterion.

[46] Thus we have a set of clear days from the field data, and another set of clear days from the atmospheric model output. These days are not necessarily the same, but it is assumed that monthly averaged vertical profiles are well comparable: in Figure 7, temperature and specific humidity from the model is compared with monthly averages of clear-sky weather balloon launches at Neumayer. Absolute differences between model and balloon profiles are plotted using dashed lines. Profiles of temperature and specific humidity at other locations in other months show similar agreement. The balloon and model profiles of temperature differ by at most 3.1 K , and water vapor concentrations by 270 ppmV at the surface. Broadband surface albedo calculated with the balloon sounding data is only 0.001 larger than in the case with RACMO2/ANT model profiles, so application of the model profiles is justified.

4.3. Observed Monthly Averaged Albedo

[47] Monthly averages of observed broadband clear-sky albedo for all locations are plotted in Figure 8. To a varying

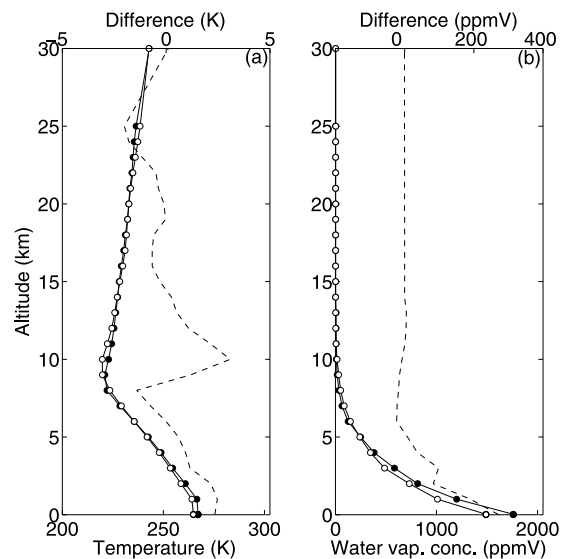


Figure 7. Monthly averaged vertical atmospheric profiles of (left) temperature and (right) water vapor from (solid dots) Neumayer balloon data and (open dots) RACMO2/ANT model output. The dashed lines are the difference between balloon and RACMO2/ANT data, with corresponding scales on the upper x-axes. Shown here are the average January profiles for clear days.

extent, the albedo decreases from October to January and increases from January to March. Part of this behavior can be explained by the annual cycle in daily averaged θ_0 , but there are other effects playing a potentially important role: (1) in summer it will be warmer, so that snow metamorphism can take place faster. Moreover, temperature gradients in the snowpack are likely larger, which has been shown to be of key importance too [Flanner and Zender, 2006]. The average snow grain size could therefore vary strongly, which influences albedo (we will show in section 4.4 that this is a major effect); (2) the vertical water vapor column in the atmosphere increases in the summer months, which is a counteracting

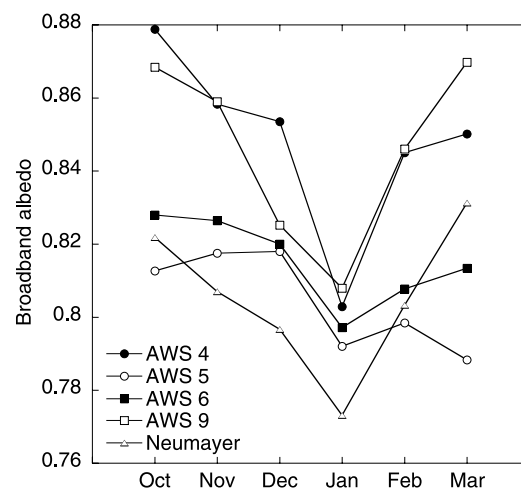


Figure 8. Average monthly values of observed clear-sky broadband albedo.

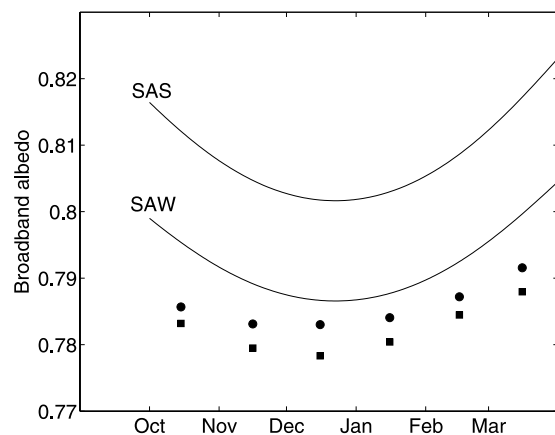


Figure 9. Modeled broadband albedo as a function of month (and hence, θ_0). The solid lines represent calculations for a constant standard subarctic summer (SAS) and subarctic winter (SAW) atmosphere. The solid squares (AWS 6) and dots (AWS 4) are model calculations using RACMO2/ANT monthly averaged atmospheres. Snow grain size is constant at $100 \mu\text{m}$ in this figure.

effect as it increases albedo in the summer months. Using DAK for the snow and atmosphere, we can disentangle the effects of variations in θ_0 , r_e , and water vapor content on the observed albedo, as described in the following paragraph.

4.4. Albedo Variations and the Role of Snow Grain Size

[48] Taking the atmospheric profiles from RACMO2/ANT, and calculating the monthly averaged θ_0 for every location, we can calculate the model broadband surface albedo. Monthly values of θ_0 are calculated by averaging hourly values of θ_0 weighted by SW_{\downarrow} .

[49] First, we assess what the influence of the annual variation in water vapor concentration is on the surface albedo. This is shown in Figure 9 as solid squares (AWS 6) and dots (AWS 4). The solid squares and dots represent model calculations in which monthly averaged atmospheric profiles from RACMO2/ANT are adopted. The lines in Figure 9 represent theoretical surface albedo at AWS 6 for a standard subarctic summer (SAS) and winter (SAW) atmosphere and a constant r_e of $100 \mu\text{m}$. The albedos calculated with RACMO2/ANT atmospheres are lower than the SAS and SAW atmospheres since the water vapor column in the RACMO2/ANT atmospheres is thinner. The fact that the RACMO2/ANT curve is flatter than the SAS and SAW curves shows the effect of seasonal variations in water vapor concentration, which is only minor (<0.005). The spatial effect (thicker atmospheres and lower θ_0 at the coast than inland) is larger ($0.005-0.01$), as is shown by the solid dots in the same figure for AWS 4.

[50] Second, the influence of the snow grain size r_e is assessed. For a range of snow grain sizes, model calculations of albedo have been made using location-specific atmospheric profiles and θ_0 . An example of these calculations is shown in Figure 10 for Neumayer. The curves shown in Figure 10 would be the broadband albedo at AWS 9 if r_e would remain constant. Now that θ_0 and the state of the atmosphere have been fixed, there is only one variable in the model that can be adjusted to make the

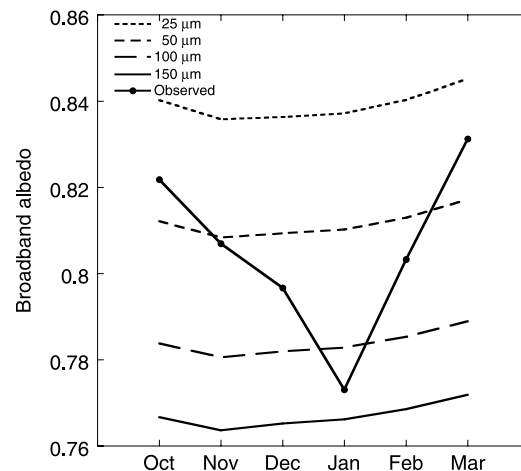


Figure 10. Calculated seasonal cycle of broadband albedo for Neumayer for several constant values of snow grain size r_e . The variations in atmospheric conditions and solar zenith angle have been taken into account. The solid line with dots represent measured values of monthly mean clear-sky albedo at Neumayer.

model and observations agree: the snow grain size r_e . We can deduce the snow grain size for each measured value of monthly averaged albedo by varying r_e until model result and observation are the same. The result for all locations is shown in Figure 11. A common feature is the seasonal variation in r_e at all stations, with higher values of snow grain size in January. This is likely due to enhanced snow metamorphosis at higher temperatures. From Neumayer via AWS 5 and 6 to AWS 9, there is a decrease in snow grain size from the coast to the plateau. A peculiar exception to this is AWS 4. The high albedo there may be attributed to a combination of very frequent snow fall (totaling $\sim 390 \text{ mm w.e. a}^{-1}$), rime formation on the surface due to frequent fog, and fairly low

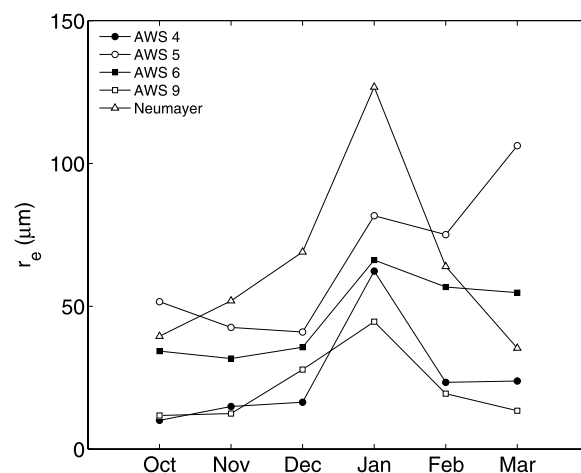


Figure 11. Average monthly values of snow grain size r_e (μm) determined from observed clear-sky albedo. With these values for r_e , model and observations are in agreement, taking into account the effects of seasonally varying θ_0 and atmospheric profiles.

temperatures due to its southward location well away from the coast. All these conditions hint to the fact that snow grain sizes may be very low on average.

[51] The albedo at AWS 5 and 6 does not rise after January, and this implies larger snow grains even in late summer. This may be coincidental: snowfall accumulation is confined to a few big events per year, and from 1998 to 2001, these events did not occur between January and March [Van den Broeke *et al.*, 2004b]. The surface snow grains can therefore continue to grow.

5. Discussion

[52] In analyzing the drivers of snow albedo variations, some assumptions have been made. Some of these assumptions were necessary because of the design of the radiative transfer model (e.g., that the surface is flat) and some were made because they are judged to make no significant changes to the main conclusions (e.g., that soot concentrations are negligibly small). We will briefly touch upon various of these assumptions.

5.1. Soot

[53] Soot concentrations have been assumed to be negligible. Soot concentrations are allegedly low in Antarctic snow, except perhaps downwind from research stations where locally produced soot may have contaminated the snowpack [e.g., Warren and Clarke, 1990]. Atmospheric concentrations of black carbon (BC) measured at Neumayer are very low (in the order of 2 ng m^{-3} [R. Weller, personal communication, 2008]), suggesting that neglecting any impurities in the snowpack is reasonable, certainly for the remote AWSs.

5.2. Sastrugi and Wind Ripples

[54] When the sun azimuth is aligned perpendicular to wind ripples and sastrugi at the snow surface, measured values of albedo can differ up to 4% from the situation in which sastrugi and solar azimuth are aligned parallel [Carroll and Fitch, 1981]. This effect tends to average out when sufficiently large spatial and temporal averages are considered [Grenfell *et al.*, 1994]. In our case, sastrugi are relatively small-scale features in comparison to the field-of-view of the pyranometers (typically 600 m^2 for an instrument level of 2.5 m above the surface). Moreover, sastrugi constantly change their location and orientation. Sunlit and shadowed fractions of the surface due to sastrugi will be evenly represented in the instrument field-of-view for monthly averages of albedo as we use in this study.

5.3. In Situ Validation of Snow Grain Size

[55] Although the seasonal variation in snow grain size that we found is realistic and plausible, it turns out to be very difficult to independently verify whether this annual variation in snow grain size is realistic: information about r_e at the measurement locations is nonexistent. Recent accounts of snow grain sizes in the area are found in Gay *et al.* [2002] and Kärkäs *et al.* [2002] but are not readily convertible to an optically equivalent snow grain size due to different measurement techniques or different definitions of snow grain size.

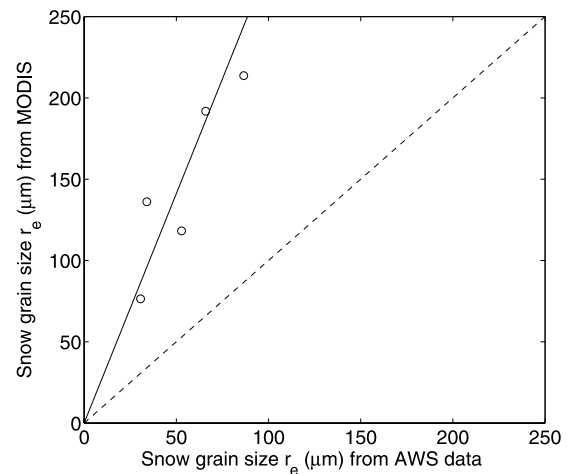


Figure 12. Snow grain sizes obtained from AWS data (Dec.–Feb. averages) on the horizontal axis, compared to MODIS-derived snow grain sizes (vertical axis). The solid line, having a slope of 2.81, is a linear fit to the data points forced through the origin.

[56] Recent work from Scambos *et al.* [2007], using radiances from the MODIS satellite sensors to retrieve snow grain size, suggests that summer-averaged (DJF) grain sizes range from $76 \mu\text{m}$ at AWS 9 to $213 \mu\text{m}$ at Neumayer. A comparison between our results and the MODIS-derived snow grain sizes (both averages for the Dec.–Feb. period) is shown in Figure 12. Although there is a good correlation between the two, the MODIS-derived r_e is more than twice as large. The MODIS product calculates one value for r_e from images obtained throughout the summer: it therefore implicitly assumes that r_e is constant throughout the year. It could therefore be that Scambos *et al.* [2007] obtain larger snow grains when there is a bias toward January scenes; or that in the months in which the MODIS product was acquired (Dec. 2003–Feb. 2004), snow grains were on average larger. More research is required to explain the discrepancy.

5.4. Inclination of the Snow Surface

[57] A small inclination of the surface can have a large impact on measured albedo, especially at large θ_0 . In the case of daily or monthly averages, only the tilt component in the N–Z direction is affected (see Grenfell *et al.* [1994] for example calculations). Large-scale tilt at all stations happens to be approximately in the N–Z direction, varying from very small ($<0.1^\circ$ at Neumayer, AWS 4 and 9) to 1.5° at AWS 6. However, these are values derived from large-scale digital elevation maps, and only true on scales of several kilometers. Actual values for the surface in the sensor field-of-view are in fact unknown, but likely smaller than 1° in any direction, because any larger slope would be clearly detectable in the field. As a worst case scenario calculation, we suppose a slope of 1° and $\theta_0 = 80^\circ$. The daily mean albedo is then off by 1.8% and errors in the inferred values of r_e would, in this case, be roughly 40%. This error decreases rapidly for lower θ_0 and flatter surfaces. For a slope of 0.1°

and $\theta_0 = 80^\circ$, the error in albedo decreases to 0.2% and the error in r_e would be 4%.

6. Summary and Conclusions

[58] In this paper, we have used a radiative transfer model DAK for calculating the albedo of snow surfaces, which is based on a combination of the correlated k -distribution technique for gas absorption and the accurate doubling-adding method for multiple scattering in the atmosphere and the snowpack. The model calculates radiative transfer in a snow–atmosphere system for shortwave radiation in 29 wavelength intervals. It can handle different types of snow particles, cloud cover (not assessed in this paper), atmospheric gas profiles, as well as soot in the snowpack (not presented here).

[59] The model performance has been demonstrated by presenting the sensitivity of both spectral and broadband albedo to variations in the solar zenith angle, snow particle size, and water vapor concentration.

[60] Our radiative transfer model has been applied to a 4-year data set of solar radiation and snow albedo, recorded at Station Neumayer and four AWSs in Dronning Maud Land, Antarctica. From these data sets, clear-sky subsets were extracted using the longwave radiation balance as a criterion. Application of the model has revealed that the annual cycle in observed broadband snow surface albedo at clear days cannot be explained by variations in the solar zenith angle alone, but that varying snow grain size must have influenced the temporal differences in albedo. These temporal differences are a robust finding. The seasonal variation in water vapor concentration at a given location turns out to play a minor role. Spatial differences in atmospheric composition (water vapor content) can cause more significant differences in albedo, however.

[61] An inherent limitation in our current application of the model is that reasonably, only longer timescale variability can be assessed and interpreted. If the model is to be used on short time scales (daily or even hourly variations), better and more measurements need to be available in a high temporal resolution. For all radiation measurements, and for unmanned AWSs even more so, it is difficult if not impossible to quantify the effects of wind and snow drift on the radiation balance. One improvement in the model snowpack would however be the incorporation of snow metamorphism laws, on the lines of *Flanner and Zender* [2006]. It would make the model more effective on the short time scales.

[62] The application of this method is not strictly limited to East Antarctica – it does apply to dry-snow surfaces in general, as long as reliable shortwave radiation measurements are available. Soot and dust concentrations can be prescribed. Practical applications will include East and West Antarctica, the dry-snow zone of Greenland, and spring snow cover on other ice caps and tundras, but exclude surfaces with melt, heavy undulations, patchy snow, or ice surfaces.

[63] With a growing contribution of remote sensing to the study of solar radiation in the snow–atmosphere system, it is of great importance to apply a uniform method of ground-truthing of snow properties. In the absence of this, we have shown that estimates of, and trends in, snow grain size can be obtained by combining model calculations with field meas-

urements of radiative fluxes. A next step would therefore be to apply DAK to a data set where all parameters relevant to albedo variations, including direct measurements on snow grain sizes, are measured simultaneously. In this way, a “closure” of the model can be achieved.

[64] **Acknowledgments.** We would like to thank Elise Hendriks for the program code for treating impurities in the snowpack; Hans Oerter and Rolf Weller for discussing snow density and impurity data; Ted A. Scambos for discussing snow grain size variations; Willem Jan van de Berg for providing RACMO profiles; and various colleagues for valuable discussions. Mark Flanner and two anonymous referees are kindly thanked for their constructive comments.

References

- Anderson, G. P., S. A. Clough, F. X. Kneizys, J. H. Chetwynd, and E. P. Shettle (1986), AFGL atmospheric constituent profiles (0–120 km), *Tech. Rep. AFGL-TR-86-0110*, Air Force Geophysics Laboratory, Hanscom, MA.
- Aoki, T., T. Aoki, M. Fukabori, and A. Uchiyama (1999), Numerical simulation of the atmospheric effects on snow albedo with a multiple scattering radiative transfer model for the atmosphere–snow system, *J. Meteorol. Soc. Jpn.*, *77*(2), 595–614.
- Carroll, J. J., and B. W. Fitch (1981), Effects of solar elevation and cloudiness on snow albedo at the South Pole, *J. Geophys. Res.*, *86*(C6), 5271–5276.
- De Haan, J. F., P. B. Bosma, and J. W. Hovenier (1987), The adding method for multiple scattering calculations of polarized light, *Astron. Astrophys.*, *183*, 371–391.
- De Rooij, W. A., and C. C. A. H. van der Stap (1984), Expansion of Mie scattering matrices in generalized spherical functions, *Astron. Astrophys.*, *131*, 237–248.
- Flanner, M. G., and C. S. Zender (2006), Linking snowpack microphysics and albedo evolution, *J. Geophys. Res.*, *111*, D12208, doi:10.1029/2005JD006834.
- Flanner, M. G., C. S. Zender, J. T. Randerson, and P. J. Rasch (2007), Present-day climate forcing and response from black carbon in snow, *J. Geophys. Res.*, *112*, D11202, doi:10.1029/2006JD008003.
- Gay, M., M. Fily, C. Genthon, M. Frezzotti, H. Oerter, and J. G. Winther (2002), Snow grain-size measurements in Antarctica, *J. Glaciol.*, *48*(163), 527–535.
- Grenfell, T. C., S. G. Warren, and P. C. Mullen (1994), Reflection of solar radiation by the Antarctic snow surface at ultraviolet, visible, and near-infrared wavelengths, *J. Geophys. Res.*, *99*(D9), 18,669–18,684.
- Hess, M., R. B. A. Koelemeijer, and P. Stammes (1998), Scattering matrices of imperfect hexagonal ice crystals, *J. Quant. Spectrosc. Radiat. Transfer*, *60*(3), 301–308.
- Kärkäs, E., H. Granberg, K. Kanto, K. Rasmus, C. Lavoie, and M. Leppäranta (2002), Physical properties of the seasonal snow cover in Dronning Maud Land, East Antarctica, *Ann. Glaciol.*, *34*, 89–94.
- Kasten, F., and A. T. Young (1989), Revised optical air mass tables and approximation formula, *Appl. Opt.*, *28*, 4735–4738.
- Kato, S., T. P. Ackerman, J. H. Mather, and E. E. Clothiaux (1999), The k -distribution method and correlated- k approximation for a shortwave radiative transfer model, *J. Quant. Spectrosc. Radiat. Transfer*, *62*, 109–121.
- Knap, W. H., L. C. Labonnote, G. Brogniez, and P. Stammes (2005), Modeling total and polarized reflectances of ice clouds: Evaluation by means of POLDER and ATSR-2 measurements, *Appl. Opt.*, *44*(19), 4060–4073.
- König-Langlo, G., and A. Herber (1996), The meteorological data of the Neumayer Station (Antarctica) for 1992, 1993 and 1994, *Ber. Polarforsch.* 187, Alfred Wegener Institute for Polar and Marine Research, Bremerhaven.
- König-Langlo, G., J. C. King, and P. Pettré (1998), Climatology of the three coastal Antarctic stations Dumont d’Urville, Neumayer, and Halley, *J. Geophys. Res.*, *103*(D9), 10,935–10,946.
- Lacis, A. A., and V. Oinas (1991), A description of the correlated k distribution method for modeling nongray gaseous absorption, thermal emission, and multiple scattering in vertically inhomogeneous atmospheres, *J. Geophys. Res.*, *96*(D5), 9027–9063.
- Legagneux, L., A. S. Taillandier, and F. Domine (2006), Grain growth theories and the isothermal evolution of the specific surface area of snow, *J. Appl. Phys.*, *95*(11), 6175–6184.
- Liljequist, G. H. (1956), Energy exchange of an Antarctic snow field: Shortwave radiation (Maudheim $71^\circ 03'S$, $10^\circ 56'W$), in *Norwegian-British-Swedish Antarctic Expedition, 1949-52, Scientific Results*, vol. 2, part 1A, Norsk Polarinstitutt, Oslo.

- Macke, A., J. Mueller, and E. Raschke (1996), Single scattering properties of atmospheric ice crystals, *J. Atmos. Sci.*, 53(19), 2813–2825.
- Matzl, M., and M. Schneebeli (2006), Measuring specific surface area of snow by near-infrared photography, *J. Glaciol.*, 52(179), 558–564.
- Nolin, A. W., and J. Dozier (2000), A hyperspectral method for remotely sensing the grain size of snow, *Remote Sens. Environ.*, 74(2), 207–216.
- Ohmura, A., et al. (1998), Baseline Surface Radiation Network (BSRN/WCRP): New precision radiometry for climate research, *Bull. Am. Meteorol. Soc.*, 79(10), 2115–2136.
- Potter, J. F. (1970), The delta function approximation in radiative transfer theory, *J. Atmos. Sci.*, 27, 943–949.
- Rusin, N. P. (1961), Meteorological and radiational regime of Antarctica, *Tech. rep.*, Israel program for scientific translations, Jerusalem.
- Scambos, T. A., T. M. Haran, M. A. Fahnestock, T. H. Painter, and J. Bohlander (2007), MODIS-based Mosaic of Antarctica (MOA) data sets: Continent-wide surface morphology and snow grain size, *Remote Sens. Environ.*, 111(2–3), 242–257.
- Stam, D., J. F. de Haan, J. W. Hovenier, and P. Stammes (2000), A fast method for simulating observations of polarized light emerging from the atmosphere applied to the oxygen-A band, *J. Quant. Spectrosc. Radiat. Transfer*, 64, 131–149.
- Stammes, P. (2001), Spectral radiance modelling in the UV–Visible range, in *IRS 2000: Current Problems in Atmospheric Radiation*, edited by W. L. Smith and Y. M. Timofeyev, pp. 385–388, A. Deepak, Hampton, VA.
- Stammes, P., J. F. de Haan, and J. W. Hovenier (1989), The polarized internal radiation field of a planetary atmosphere, *Astron. Astrophys.*, 225, 239–259.
- Thomas, G. E., and K. Stamnes (1999), *Radiative Transfer in the Atmosphere and Ocean*, 1st ed., Cambridge Univ. Press, Cambridge.
- Van As, D., M. R. van den Broeke, and R. S. W. van de Wal (2005), Daily cycle of the surface layer and energy balance on the high Antarctic plateau, *Antarct. Sci.*, 17, 121–133.
- Van de Hulst, H. C. (1963), A new look at multiple scattering, *Tech. Rep.*, Inst. Space Studies, NASA, New York.
- Van den Berg, W. J., M. R. van den Broeke, C. H. Reijmer, and E. van Meijgaard (2006), Reassessment of the Antarctic surface mass balance using calibrated output of a regional atmospheric climate model, *J. Geophys. Res.*, 111, D11104, doi:10.1029/2005JD006495.
- Van den Broeke, M. R., C. H. Reijmer, and R. S. W. van de Wal (2004a), Surface radiation balance in Antarctica as measured with automatic weather stations, *J. Geophys. Res.*, 109, D09103, doi:10.1029/2003JD004394.
- Van den Broeke, M. R., C. H. Reijmer, and R. S. W. van de Wal (2004b), A study of the surface mass balance in Dronning Maud Land, Antarctica, using automatic weather stations, *J. Glaciol.*, 50(171), 565–582.
- Van den Broeke, M. R., D. van As, C. H. Reijmer, and R. S. W. van de Wal (2004c), Assessing and improving the quality of unattended radiation observations in Antarctica, *J. Atmos. Oceanic Technol.*, 21, 1417–1431.
- Van den Broeke, M. R., C. H. Reijmer, D. van As, and W. Boot (2006), Daily cycle of the surface energy balance in Antarctica and the influence of clouds, *Int. J. Climatol.*, 26, 1587–1605.
- Warren, S. G., and A. D. Clarke (1990), Soot in the atmospheric and snow surface of Antarctica, *J. Geophys. Res.*, 95(D2), 1811–1816.
- Warren, S. G., R. E. Brandt, and T. C. Grenfell (2006), Visible and near-ultraviolet absorption spectrum of ice from transmission of solar radiation into snow, *Appl. Opt.*, 45(21), 5320–5334.
- Wiscombe, W. J., and S. G. Warren (1980), A model for the spectral albedo of snow. I: Pure snow, *J. Atmos. Sci.*, 37, 2712–2733.

W. H. Knap and P. Stammes, Royal Netherlands Meteorological Institute (KNMI), Climate Research and Seismology Department, P.O. Box 201, 3730 AE De Bilt, Netherlands.

G. König-Langlo, Alfred Wegener Institute, Building F-114, Bussestrasse 24, D-27570 Bremerhaven, Germany.

P. Kuipers Munneke, C. H. Reijmer, and M. R. van den Broeke, Institute for Marine and Atmospheric Research, Utrecht University, P.O. Box 80005, NL-3508 TA Utrecht, Netherlands. (p.kuipersmunneke@uu.nl)